

Research Paper

An investigation into the porosity of extrusion-based 3D printed concrete

Jacques Kruger^{a,*}, Anton du Plessis^{b,c}, Gideon van Zijl^a^a Division for Structural Engineering and Civil Engineering Informatics, Department of Civil Engineering, Stellenbosch University, Stellenbosch, 7602, South Africa^b Research group 3DInnovation, Stellenbosch University, Stellenbosch 7602, South Africa^c Department of Mechanical Engineering, Nelson Mandela University, Port Elizabeth 6001, South Africa

ARTICLE INFO

Keywords:

3D printed concrete
 Computed tomography
 Porosity
 MicroCT
 Void characteristics

ABSTRACT

Concrete structures additively manufactured by extrusion-based 3D concrete printing are reportedly orthotropic in mechanical behavior and exhibit relative weakness in interfacial regions. Microstructure, including porosity content, 3D porosity distribution and pore morphology presents a physical basis for these phenomena. Here, a first and comprehensive microstructural investigation is reported, using X-ray computed tomography to visualize and quantify porosity, pore sizes, shapes and distributions in extrusion-based 3D printed concrete. 3D printed plastic molds are used to sample specimens from freshly 3D printed concrete filaments, for minimum disturbance. As reference, similar specimens of the exact same concrete mix, but cast without compaction, instead of being 3D printed are included in the study. A fixed diameter of 20 mm, but varying height is used to include a single filament layer (10 mm), two layers (20 mm) and four layers (40 mm). Both typical horizontal interfaces in multi-layer elements, and vertical interfaces between multilaterally deposited filaments are studied. Whilst a single 3D printable concrete mix are considered, print variables of pass time (0–60 min with 15 min intervals) and print speed (80, 100 and 120 mm/s) are considered to investigate their potential alteration of the microstructure. Findings are significant, indicating tri-axial spheroid shaped air voids present in printed specimens, elongated and flat in the print direction, compared to mostly spherical voids in cast specimens. This prompts for more research to be conducted into the effect of stress concentrations at micro-cracks or voids in 3D printed concrete, which especially impacts mechanical behavior. Furthermore, it is found that vertical and horizontal interlayers comprise of similar porosity, and that it is inaccurate to qualify the homogeneity of typically fissile 3D printed concrete elements based solely on superficial cross-sectional photographic evidence from saw-cut samples.

1. Introduction

3D concrete printing (3DCP), or digital fabrication with concrete, is reforming the construction industry into a modern, digitized and bespoke industry with unprecedented design and construction freedom [1]. The most widely adopted additive manufacturing method for 3DCP is currently extrusion-based printing [2], where extruded concrete filaments are deposited onto one another in a layer-wise fashion until the desired object is realized [3]. Although a highly promising technology for the field of construction, there are two principal motivations for this research. Firstly, unlike conventionally cast concrete methods where concrete is placed into formwork and vibrated to remove entrapped air, 3DCP is pumped under pressure to the nozzle and does not experience any vibration before or after deposition [4]. This could potentially result in disparities between intralayer void sizes, shapes and fractions of 3D

printed and cast concrete. A possible consequence thereof is already observed in literature, where the flexural strength of 3D printed samples with filament layers oriented horizontally (orientation I) is larger than that of conventionally cast concrete samples [5]. Secondly, lack-of-fusion between successively printed concrete filaments, which originates from air entrapment or enclosure during filament-on-filament deposition [6] and/or water migration between filaments [7] due to surface moisture evaporation during printing [8,9], typically yields weak interlayer bonding with consequential effects [10]. Severe anisotropy is the most widespread reported consequence thereof, where compressive, flexure and tensile (or interlayer bond) strengths of 3D printed concrete reduce significantly compared to homogenous conventionally cast concrete specimens [6,9,11]. Durability of 3DCP may also be compromised sooner than that of conventionally cast concrete, since recent findings reveal that chloride penetration is facilitated

* Corresponding author.

E-mail address: pjkruger@sun.ac.za (J. Kruger).<https://doi.org/10.1016/j.addma.2020.101740>

Received 22 September 2020; Received in revised form 11 November 2020; Accepted 30 November 2020

Available online 5 December 2020

2214-8604/© 2020 Elsevier B.V. All rights reserved.

via the interlayers [12,13], thus presenting evidence for potentially increased corrosion rates of reinforced 3DCP [14,15]. Preliminary investigations indicate structural fire performance of 3D printed concrete is also affected by weak interlayers, where self-equilibrating thermal stresses cause delamination of concrete filaments at elevated temperatures [16,17].

At the origin of all these consequences is porosity, particularly the void fractions, sizes, shapes, interconnectivity, distribution and positions, both within the filament (intra) and in-between (inter) layers. Preliminary evidence, in the form of a micro computed tomography (CT) investigation into 3D printed concrete porosity depicted in Fig. 1, portrays visual disparities between printed and cast concrete porosity and therefore warrants further investigation [17]. Furthermore, a recent study investigated via CT scanning and mechanical testing the correlation between pore characteristics and tensile bond strength of printed concrete [18]. The authors found higher porosity present in interlayer regions, but that only four of their ten samples failed under tensile loading at the corresponding interlayer position of highest porosity, indicating there are other factors in addition to only total porosity affecting the mechanical behavior of 3D printed concrete. Porosity in concrete plays a role in water transport and hydration, also in traditional cast concrete [19]. However, unlike cast concrete, the porosity in 3D printed concrete is not homogeneously distributed due to the extrusion process and may vary in its size distribution which is expected to affect the material properties [20,21]. Quantification of this distribution in 3DCP porosity may therefore significantly enhance the fundamental comprehension of plausible mechanisms that induce failure between concrete filaments and subsequently aid with the development of appropriate solutions thereto. X-ray CT technology is utilized in this paper to this end, based on the successful application thereof in previous studies conducted on conventionally cast concrete and asphalt [22], as a first attempt toward holistic characterisation of a 3D printable cementitious material's porosity (including pore shape, size, distribution, orientation and position). CT technology is widely used in additive manufacturing, with its largest application being the quantification of porosity in metal additive manufacturing [23]. In this work the authors set out to visualize and quantify the porosity characteristics in 3D printed concrete. Samples are obtained from 3D printed, high-performance mortar filaments to investigate 1) the intralayer porosity compared to that of conventionally cast concrete, 2) horizontal interlayer porosity between two successively deposited filament layers, 3) vertical interlayer porosity between two laterally deposited filament layers and 4) the porosity distribution over four successively deposited filament layers. The paper presents the results from this experimental campaign both qualitatively and quantitatively, discusses the potential mechanisms responsible for the observed porosities and reports conceivable recommendations based on the analysis of the study's results.

2. Materials & methods

2.1. 3D printable mortar composition and properties

The 3D printable mortar employed in this research is the standard high-performance mortar utilized by Stellenbosch University's 3DCP research team [24]. The mix ingredients and proportions are given in Table 1. A low water-to-cement (w/c) ratio of 0.45 is used, yielding significant hardened concrete state mechanical properties. A polycarboxylate ether (PCE) superplasticizer, namely Chryso Premia 310, is used to obtain appropriate workability in the fresh concrete state, i.e. pumpability, extrudability and thixotropy, suitable for 3DCP at such low w/c ratio. The binder consists of a CEM II/A-L 52.5 N normal hardening cement with between 6% and 20% limestone substitution, DuraPozz class F fly ash and Chryso densified silica fume (DSF) as extenders to aid with obtaining improved rheology and hardened state properties. A locally mined fine Malmesbury aggregate is used as filler, with a maximum particle size of 4.75 mm and exhibiting a continuously graded particle-size distribution. Common potable tap water is added to the dry materials during mixing in a two-blade pan mixer.

The 3D printable mortar typically has a 28-day cast cube compressive strength of around 70 MPa and Young's Modulus of around 30 GPa [25]. The interlayer bond strength of a printed sample with filament layers oriented vertically, tested in four-point flexure, is typically about 6.8 MPa with a pass time similar to what will be used in this study of 30 s, compared to the 8.4 MPa flexural strength of a cast sample. In terms of 3DCP buildability, the material achieves a height of 600 mm in 13 min, yielding a vertical build rate of 45.5 mm/min (or 2.73 m per hour), despite the short print path for a $\varnothing 250$ mm circular hollow column [26]. This is based on a static and dynamic yield stress of 2995 and 678 Pa respectively, a re-flocculation rate of 6.7 Pa/s (i.e., relatively high thixotropy) and a structuration rate of 1.1 Pa/s (normal setting). The material has an initial setting time of roughly 210 min

2.2. Sample preparation & configurations

Small cylindrical samples with $\varnothing 20$ mm and varying heights are

Table 1
3DPC mix constituent quantities.

Constituent	Description	kg
Cement	PPC SureTech 52.5 N	579
Fly Ash	DuraPozz Class F	165
Silica Fume	Chryso DSF	83
Fine Aggregate	Local Malmesbury	1167
Water	Potable Tap Water	261
Superplasticizer	Chryso Premia 310	5.75

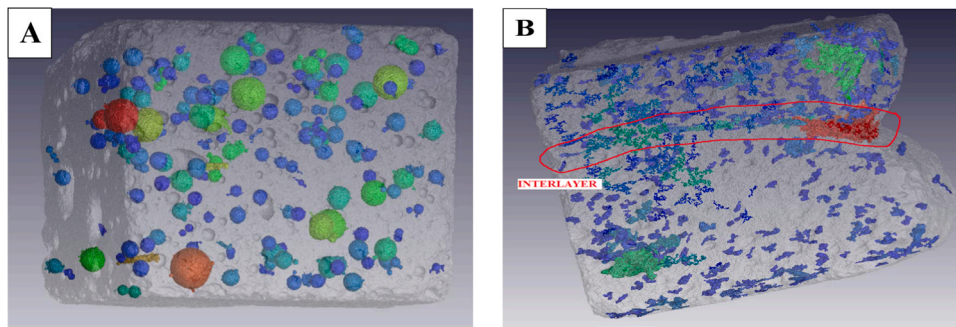


Fig. 1. A preliminary micro CT investigation illustrating clear disparities in void characteristics between A) conventionally cast concrete and B) 3D printed concrete comprising of two filaments and one horizontal interlayer [17].

Figure reprinted from the Fire Safety Journal, 103075, Antonio Cicione, Jacques Kruger, Richard Walls, Gideon van Zijl, An experimental study of the behavior of 3D printed concrete at elevated temperatures, In Press, 2020, with permission from Elsevier.

prepared to attain high CT scanning resolutions. As outlined in [27], the porosity of typical cast concrete extends across multiple size ranges from mm to nm scales. Micro CT scans at 20 μm voxel size, which is attained at high quality for 20 mm samples, allows to provide good quantitative evaluation of pores $> 60 \mu\text{m}$ in diameter (3 voxels), while giving a reasonable representative volume (field of view). The samples are extracted from the center of mortar filaments (or tracks), which were printed using a gantry-type 3D concrete printer at 16 °C and 40% relative humidity climate conditions. The concrete printer has a build volume of roughly 1 m³ with three translational degrees of freedom, paired together with a progressive cavity pump for material transport. The pass time is kept sufficiently low to reduce the likelihood of surface water evaporation between layer depositions. An 80 mm/s print speed, together with a $\varnothing 25$ mm circular nozzle, are used to yield a 10 mm layer height and approximately 35 mm layer width. In unison with a 10 mm deposition height and approximately 29 cm³/s material flow/extrusion rate, compaction overlay is attained where filaments are squeezed onto one another to improve interlayer bond strength [28]. Disposable molds are 3D printed using polylactic acid (PLA) thermoplastic and the Creality CR-10 Max 3D printer for accurate sample preparation. This negates any saw-cutting that may unknowingly influence the microstructure (e.g. causing cracks) during sample extraction and hence affect the CT results. These molds are then pressed into the mortar filaments 2 h after print completion, which is the period in which most plastic shrinkage has occurred for this 3D printable concrete [29]. Hereby, the mortar microstructure is not significantly impacted by the mold insertion and curing process and should yield consistent microstructures. The print path direction is indicated on top of each sample by an arrow, in order to aid with data analysis and interpretation. The samples were left intact on the print bed for the first 24 h after printing as to not influence the hydration process and thus early concrete microstructure formation. Samples are demolded after 24 h using a side cutting plier and cured in climate-controlled conditions at 23 °C and 65% relative humidity for 28 days. Thereafter, the samples undergo CT scanning. Full filament samples, consisting of both single and multiple filaments, are also extracted from the 3D printing process. These samples were not obtained via molding, but rather cut to length whilst in the plastic concrete state. Fig. 2 shows the samples while both in molds (for illustrative purposes only) and after being demolded. The exact influence of mold usage for sample preparation on porosity is unknown to the authors; however, at minimum it ensures for consistency between test configurations and subsequent comparison. Regions close to the mold walls were not investigated via CT scanning, to negate accounting for any possible friction influence that the mold insertion process may have on the specimen's microstructure.

Multiple test configurations are considered and investigated, as depicted in Table 2. Three samples of each configuration are prepared and CT scanned. The cast samples comprise of the same 3D printable mortar material as the other configurations; however, they did not experience any pumping or vibration. The D20H10C and D20H10P samples are investigated and the porosity results juxtaposed in order to observe inconsistencies in void fractions, sizes, and shapes between cast and printed concrete. A single printed filament segment of 40×40×10 mm (TRAC) is also investigated to determine principal void orientations. The porosity in vertical interlayers, i.e. between two laterally printed filaments, is investigated via the D20H10PV samples. The D20H20PH samples, similar to the D20H10PV samples, are employed to investigate porosity between conventional successively printed filament layers, however with interlayers oriented horizontally. Different pass times of 0, 15, 30, 45 and 60 min are employed and investigated for this configuration. The water mass loss in printed specimens due to evaporation was measured as a low $0.04 \pm 0.02 \text{ kg/m}^2/\text{h}$, which is given here to present an indication of the severity associated with the respective pass times. The D20H40PH samples are investigated to determine the porosity distribution over multiple filament intra- and interlayers. Lastly, three filaments are printed on top of one another at various print speeds (VEL), the first at 80 mm/s, the second at 100 mm/s and the third at 120 mm/s, mainly to investigate any microstructural porosity discrepancies.

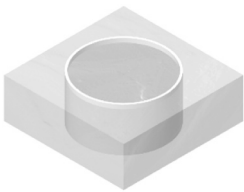
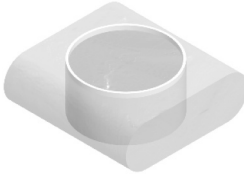



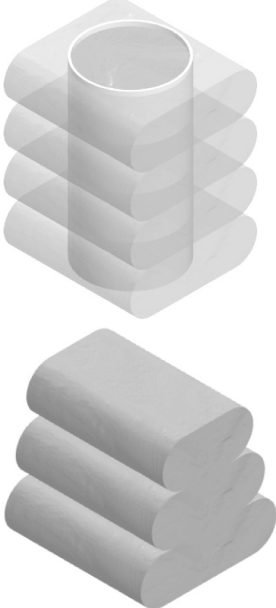
2.3. CT scanning methodology

X-ray CT was performed using a GE Nanotom S scanner, with data analysis using Volume Graphics VGSTUDIO MAX 3.4. Scans were performed at 15 μm voxel size, using 140 kV and 90 μA for X-ray generation, and 2400 images recorded in one full rotation of the sample. Porosity analysis was performed using a simplified method [30], briefly described here. The data is de-noised using an Adaptive Gauss filter, followed by a surface determination to find the exterior surface of the sample. A thin layer of 2 voxels all around the surface is removed to eliminate possible edge errors, then a new determination is made inside the material of the precise transition between pore space and solid material. This step makes use of a semi-automated local optimization which removes some potential human bias in the threshold selection. This segmentation is used as a basis for a defect analysis function, making use of the segmentation only and not any algorithm, also improving reproducibility. In addition to providing total porosity volume fraction, each individual pore space is listed with its volume, surface area, maximum diameter, compactness, projected size in each axis, etc. Compactness is defined as the ratio of the volume of the pore over



Fig. 2. Various samples extracted from 3D printed concrete filaments whilst still in their molds (white, 3D printed PLA plastic molds) and demolded before undergoing CT scanning. A numbering system is used to keep record of the respective samples while an arrow is drawn on each sample to indicate the print direction.

Table 2Sample configurations and details regarding the respective μ -CT investigations.

Configuration Name	Description	CT Investigation	Sample Illustration
D20H10C	Sample obtained from casting	Compare cast vs printed concrete porosity (void fractions, sizes, shapes)	
D20H10P	Sample obtained from one filament		
TRAC	A $40 \times 40 \times 10$ mm filament segment	Determine principle void orientations	
D20H10PV (pass time ~ 0 min)	Sample obtained from two filaments with interlayer vertical	Compare porosity between lateral filaments	
D20H20PH (pass times 0/15/30/45/60 min)	Sample obtained from two filaments with interlayer horizontal	Compare porosity between top and bottom filaments	
D20H40PH (pass time ~ 0 min)	Sample obtained from four filaments with interlayers horizontal	Compare porosity over multiple filament layers	
VEL (pass time ~ 0 min)	Three filaments printed at 80, 100 and 120 mm/s respectively	Investigate any microstructural porosity discrepancies	

the volume of a perfect sphere fitting around the pore – the circumscribed sphere. Therefore, an ideal spherical pore space will have a compactness value of 1. In this work an integration mesh was applied to provide mean porosity values in selected planes and to present the average porosity in 0.1 mm planar slices across the height of the sample. Projected size in X, Y and Z directions is used in this study to indicate shape changes relative to the print direction for the pores – the projected size recorded is that of a bounding box around the pore in the coordinate system used. Differences between pore relative sizes in X, Y and Z statistically across all pores indicate directionality and elongation.

3. Results and discussions

3.1. Cast vs printed concrete porosity

The μ -CT scan results of the mold-cast and 3D printed concrete specimens (D20H10C & D20H10P) are depicted in Figs. 3 and 4, respectively. The porosity was, on average, measured as 6.8% for the mold-cast specimen and 7.9% for the 3D printed specimen, as depicted in Fig. 5, together with coefficients of variation (COV) of 8.9% and 7.9%, respectively. Interestingly, the interlayers at 0 min pass time have almost negligible influence on printed concrete's total porosity. These results are, however, only indicative of the overall porosity in mold-cast and 3D printed concrete, since small specimens were extracted at randomly chosen positions in the concrete and may not generally exhibit bulk concrete properties. For this reason, the TRAC specimens' total porosity is also reported since a larger volume of filament is CT scanned compared to the molded specimens. It was found that these samples constitute an average porosity of 4.2%, which is almost half than that of the 3D printed, molded specimens, together with a COV of 30.9%. Although less total porosity is now measured for the printed concrete compared to the cast concrete, it should be noted that a larger voxel size of 22.5 μ m was employed for the TRAC specimens' CT scanning due to their larger size. This implies that the smaller voids measured at 15 μ m voxel size in the molded specimens cannot be measured in the TRAC specimens. Therefore, it is incorrect to compare the total porosity of the smaller specimens to that of the larger specimens. However, considering supplementary specimen data in Fig. 11, a porosity of approximately 8% seems accurate for 3D printed concrete in this research. This result is interesting considering that it is generally anticipated that the porosity of 3D printed concrete would reduce due to the pressure experienced during pumping [31]. A study by Le et al. [5] concluded that their

printable mixture contains a porosity of 3.8% and 1% for mold-cast and well-printed specimens, respectively. Similarly, van der Putten et al. [9] measured approximately 3% porosity in their 3D printable mixture. However, it should be noted that both studies made use of a 2D surface analysis technique for porosity determination and is thus not comparable to the 3D volumetric analysis conducted in this research. Kloft et al. [32] measured a mean air void content of 3.4% for their extruded 3D printable mixture using μ -CT at 36 μ m voxel size. Lee et al. [18] measured a higher mean porosity of between 5% and 6% for their printable mixture using μ -CT at 70 μ m voxel size. Noting that a higher scanning resolution was employed in this research (15 μ m for D20H10C, D20H10P and 22.5 μ m for TRAC), higher porosity values are expected compared to that of the studies presented from literature. This is indeed the case where both D20H10P and TRAC specimens possess mean porosities of 7.9% and 4.2%, respectively.

By further inspection, it can be observed that the mold-cast concrete voids seem more spherical (typical) than that of the 3D printed concrete, which possesses many small and irregular shaped voids. These voids, on average, also seem larger in volume than the mold-cast concrete's voids in specimens presented in Figs. 3 and 4. This is, however, not always the case when interpreting the comprehensive analytical data from Fig. 6. The data indicates that, for the same void diameter, mold-cast concrete's voids are generally larger in volume than that of the 3D printed concrete's voids. Note that in the case of elongated voids, the diameter is that of a sphere that encapsulates the void. This difference in void volume is almost indistinguishable at smaller diameters, but increases considerably at larger (approximately 0.3 mm in diameter) void sizes. Furthermore, the 3D printed concrete possesses significantly more voids than the mold-cast concrete that are 2 mm in diameter and larger, of which the mold-cast concrete has little to none. It is theorized that, especially in the case of the longer voids, smearing of the voids occur due to the imparted pressure from pumping while 3D printing. The larger voids then tend to elongate and smear, perhaps also reducing in size to form a few extra smaller and irregular shaped voids in the process. The opposite may also occur, where due to the relative particle movement during pumping, smaller voids link together to form larger and longer voids in the filament intralayer. Nonetheless, extruded 3D printed concrete filament contains longer and larger voids than its mold-cast counterpart in the macroscale. The largest void diameter or length measured for the mold-cast concrete specimens is 3.58 mm compared to 9.84 mm for the printed concrete specimens. Furthermore, the largest void volume measured for the mold-cast concrete specimens is 2.78 mm³

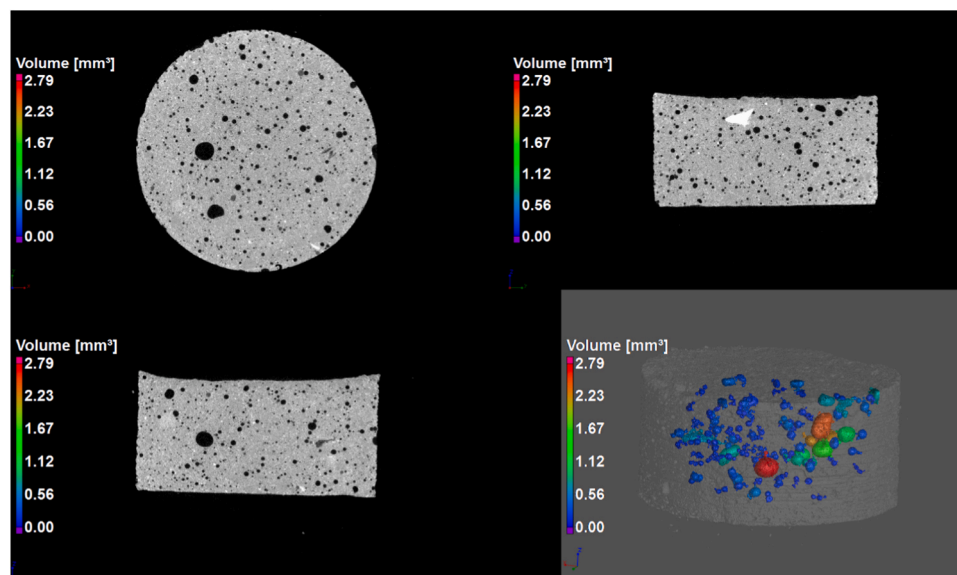


Fig. 3. The top and side CT images of the mold-cast specimen, D20H10C, as well as a 3D render indicating void positions, shapes, distributions, and volumes.

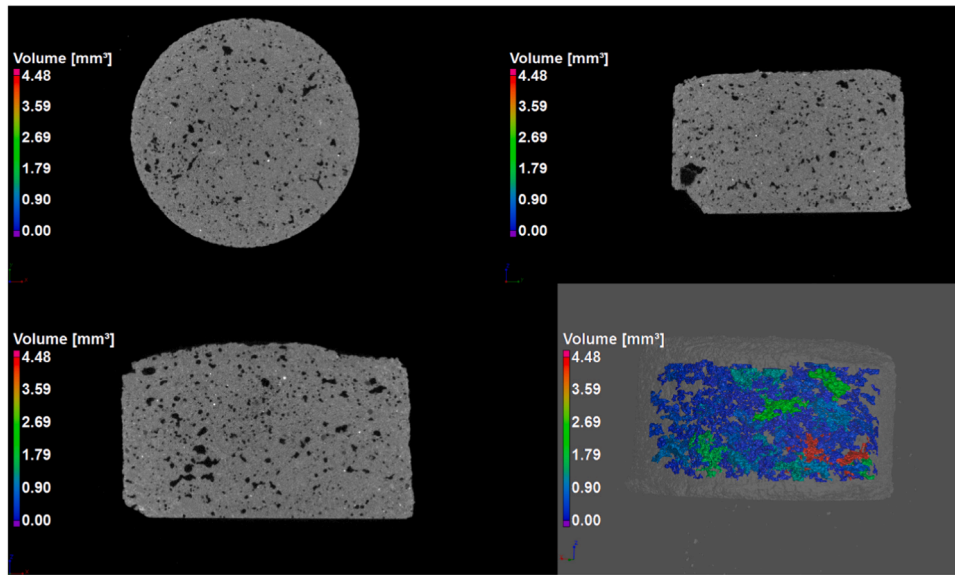


Fig. 4. The top and side CT images of the 3D printed specimen, D20H10P, as well as a 3D render indicating void positions, shapes, distributions, and volumes.

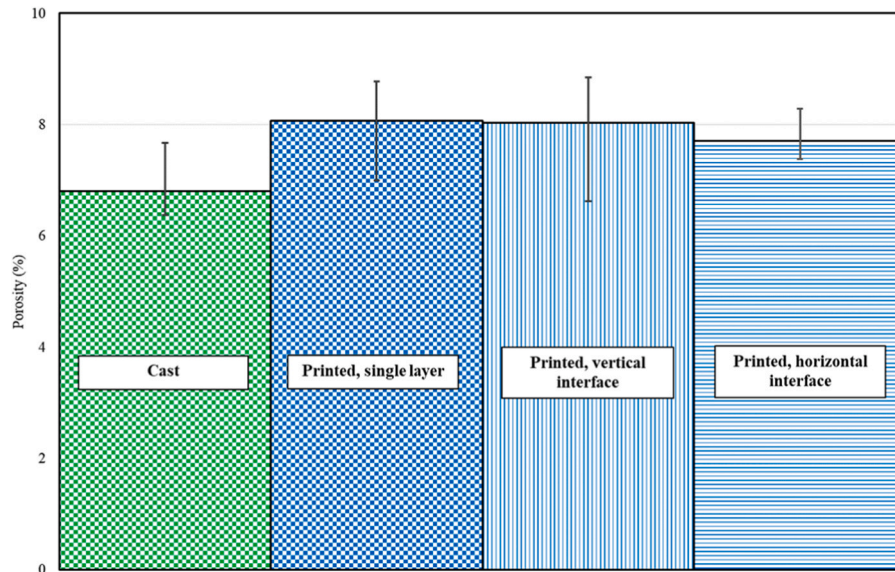


Fig. 5. Total porosity of the cast and 3D printed concrete specimens, namely D20H10C, D20H10P, D20H10PV and D20H20PH with 0 min pass time. Minimum and maximum measured values are indicated by the error bars.

compared to 9.39 mm^3 for the printed concrete specimens.

Fig. 7 depicts the compactness of the mold-cast and 3D printed concrete specimen pores. Here, compactness is determined as the volume of the measured void over the volume of a theoretically completely spherical void using the measured void's length, expressed as a unitless value between 0 and 1. Thus, a value closer to 1 indicates a completely spherical measured void. It is observed from the data that the bulk of the mold-cast concrete's voids are smaller than approximately 0.5 mm in length, with varying compactness between 0.1 and 0.7. However, an almost exponential decay is observed in the 3D printed concrete's compactness at the corresponding void diameters. At smaller voids, the compactness reaches approximately 0.6, similar to that of mold-cast concrete. This decreases to less than 0.2 for all voids larger than 1 mm in length. This presents strong evidence to suggest that the larger voids in 3D printed concrete are smeared and irregular in shape, but less so in the smaller void sizes.

To further investigate 3D printed concrete's porosity, a filament

segment (TRAC) of $40 \times 40 \times 10 \text{ mm}$ was analyzed that contains a larger sampling volume than the other small cylindrical samples (D20H10P), hence likely to yield more accurate and representative results. The results of the CT scans are depicted in Fig. 8. It is clear that the voids seem irregularly shaped and flat. From the 3D render, it can be seen that the filament comprises mostly of well-distributed, small voids of less than 1 mm in length (indicated in blue color). A few larger voids of more than 5 mm in length are present (indicated in green color), up to a maximum length of almost 13 mm in this specimen (indicated in red color). However, it should be noted that due to the irregular pore shapes, higher interconnectivity and hence permeability may possibly be obtained for printed concrete. Consequently, pores may overlap and result in larger pore sizes evident in 3D printed concrete compared to mold-cast concrete. In this specimen, the long 13 mm pore indicated in red color encompasses a volume of 29.83 mm^3 .

Supplementary material related to this article can be found online at [doi:10.1016/j.addma.2020.101740](https://doi.org/10.1016/j.addma.2020.101740).

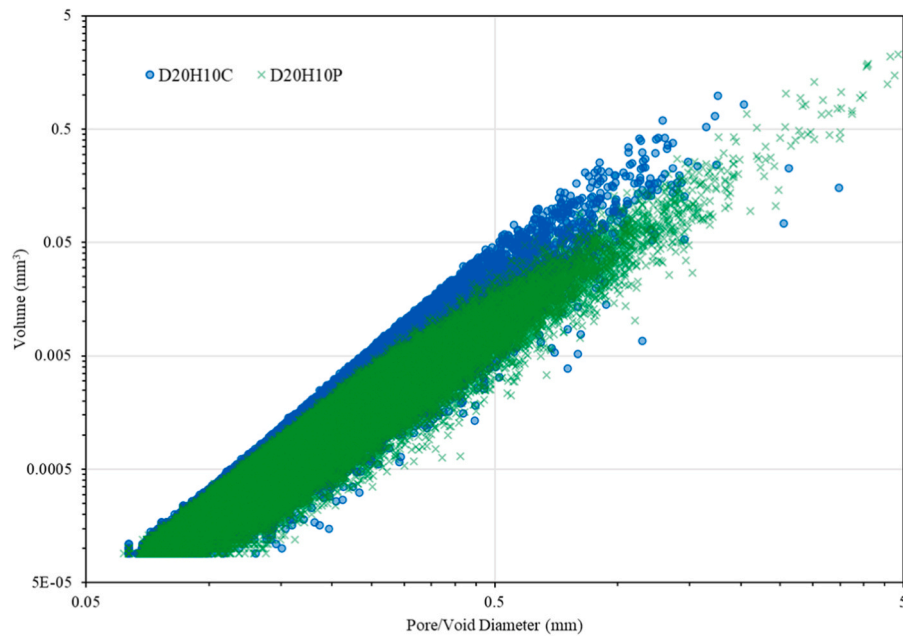


Fig. 6. Void volume comparison between mold-cast and 3D printed specimens, D20H10C and D20H10P, for a range of void diameters on a log-log plot. Pore diameter refers to the largest length of the pore space in three dimensions.

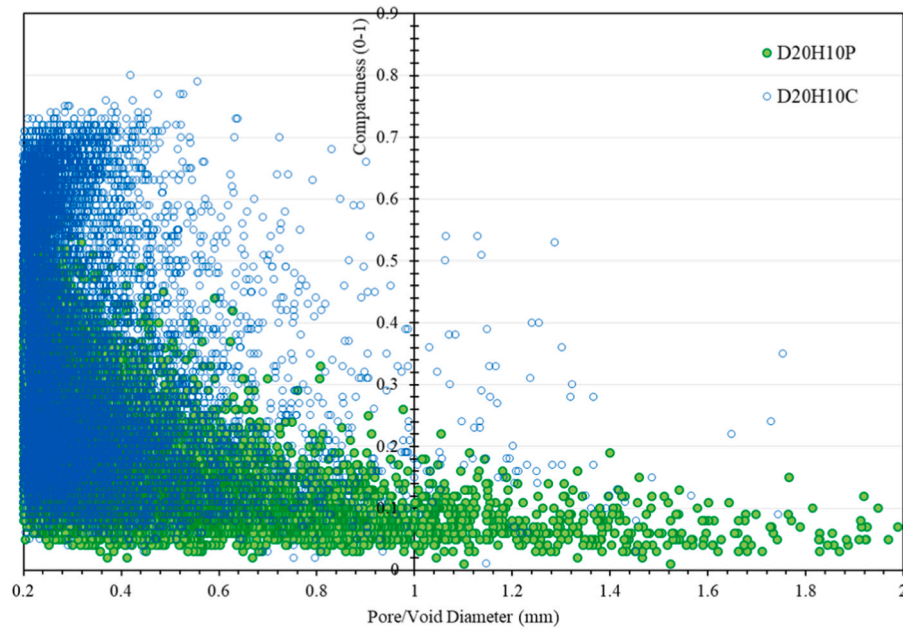


Fig. 7. Compactness comparison between mold-cast and 3D printed specimens, D20H10C and D20H10P, for a range of void diameters. Pore diameter refers to the largest length of the pore space in three dimensions.

These irregular and smeared voids evident in 3D printed concrete are further investigated by determining the voids' measurements in the three Cartesian directions, as indicated in Fig. 9. It is observed that the voids consistently measure longer in the x-direction, which corresponds to the print/nozzle direction in this research. This is followed by the distance measured in the transverse (y) direction and lastly, the smallest dimension, in the z-direction (height). The voids in extrusion-based 3D printed concrete are thus, generally, longer in the print direction and flat, and slightly wider than it is high. Together with the data from Fig. 7, it can be deduced that 3D printed concrete's voids are more tri-axial ellipsoid shaped than spherical. This may have a significant influence on especially the mechanical strength of printed concrete, since stress

concentrations may occur at sharp edges of the voids. The work of Griffith [33], who investigated fracture of brittle materials due to tensile stress concentrations at micro-crack or void corners, could be investigated as possible failure criterion for 3D printed concrete, especially in the expanded Mohr-Griffith form [34].

3.2. Horizontal interlayer porosity

The porosity between successively deposited filaments, i.e. in the interlayer regions (IRs), were investigated for pass times ranging from 0 m to 60 min. The results are depicted in Figs. 10 and 11. It is evident in Fig. 10 that the IR is almost not visible at all for the 0 min pass time.

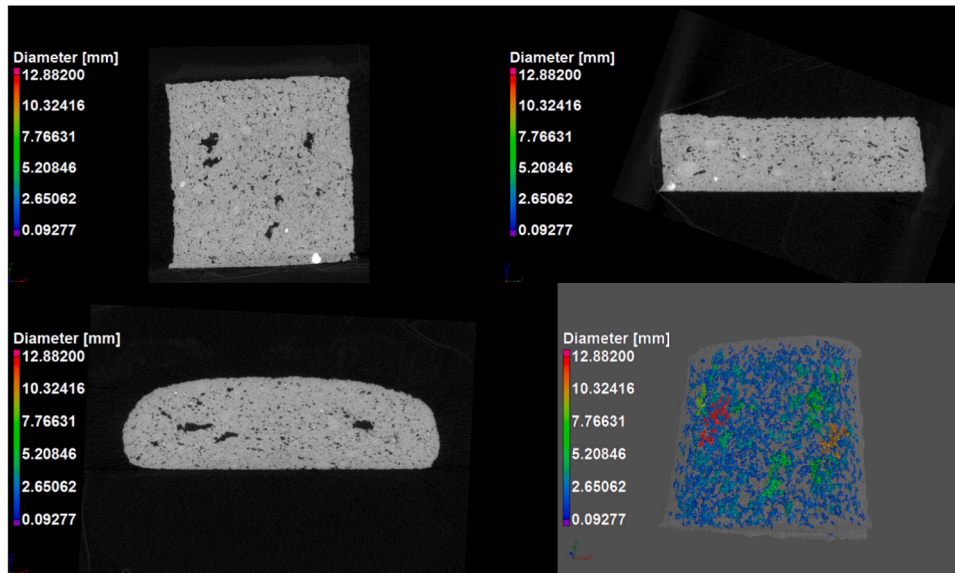


Fig. 8. The top and side CT images of the 3D printed specimen, TRAC, as well as a 3D render indicating void positions, shapes, distributions, and diameters. A supplementary Video 1 is provided for visualization of this TRAC specimen.

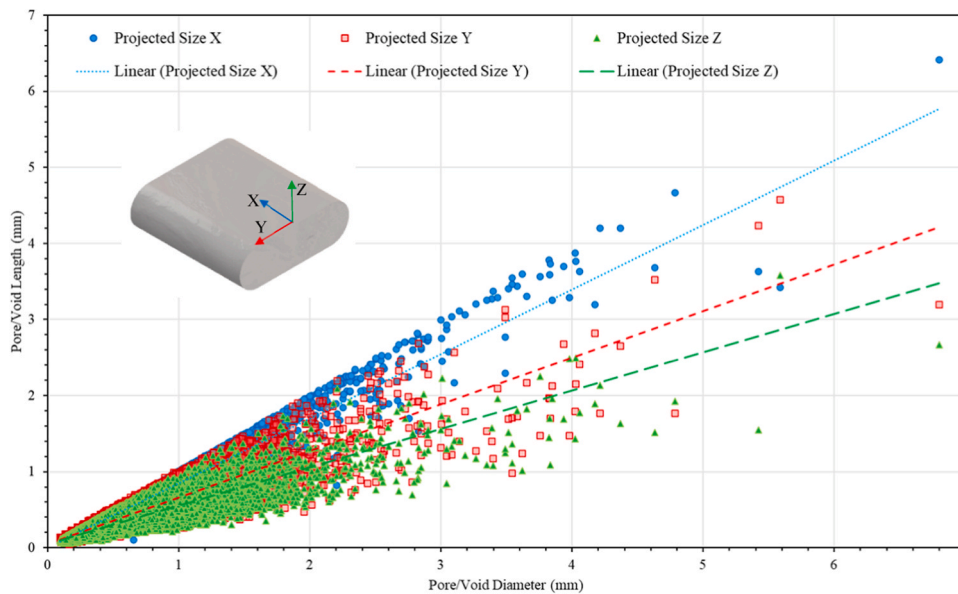


Fig. 9. Void lengths measured in the x, y, and z Cartesian directions for a range of void diameters.

This is due to minimal moisture evaporating from the filament surface, thereby preventing water migration between filaments [9]. The IR does, however, become notably more visible in the CT images as the pass time increases each 15 min up to 60 min. These IRs are also evident in the 3D porosity renders in Fig. 10. Seemingly, at shorter pass times, the IR mostly consists of many small voids. At longer pass times, the IR seems to consist of larger voids, or, many interconnected small voids that constitute one large void.

The porosity as a function of specimen height is depicted in Fig. 11 for all pass times. A stochastic porosity pattern is observed at lower pass times. In the case of 0 min, no pertinent deviation in porosity is noted at the IR, likely due to the mild water mass loss rate in the climate-controlled conditions. A peak of 12% porosity is measured approximately 6 mm below the IR; however, this corresponds with the location of the large void indicated in red in the 3D render in Fig. 10 and is not related to the IR in any manner. Roughly the same result is obtained for

15 min pass time. At a 30 min pass time, the porosity changes from 5.4% at 0.6 mm below the IR, to 9.9% at 0.5 mm above the IR. This observation is consistent with findings from literature, where higher porosity is measured above the IR due to the water migration process [10,32]. A peak of 13.7% is observed 5 mm below the IR, which coincides with the position of the large red void in Fig. 10. No clear trend is observed in the 45 min pass time specimen due to there being an increased amount of slightly larger voids throughout the intralayer (see Fig. 10). The most pronounced effect is observed in the 60 min pass time specimen, where the porosity changes from 6.9% to 14% over 0.7 mm. Although this occurred above the indicated IR on the graph, it is believed that this actually occurred over the IR itself, since the overlay map during CT scanning was not 100% aligned in the center of the specimen. On average, the intralayer porosity of 3D printable concrete in this study seems to be in the region of 8% for all pass times. It is believed from these findings that the IR consists of many small voids, which at longer

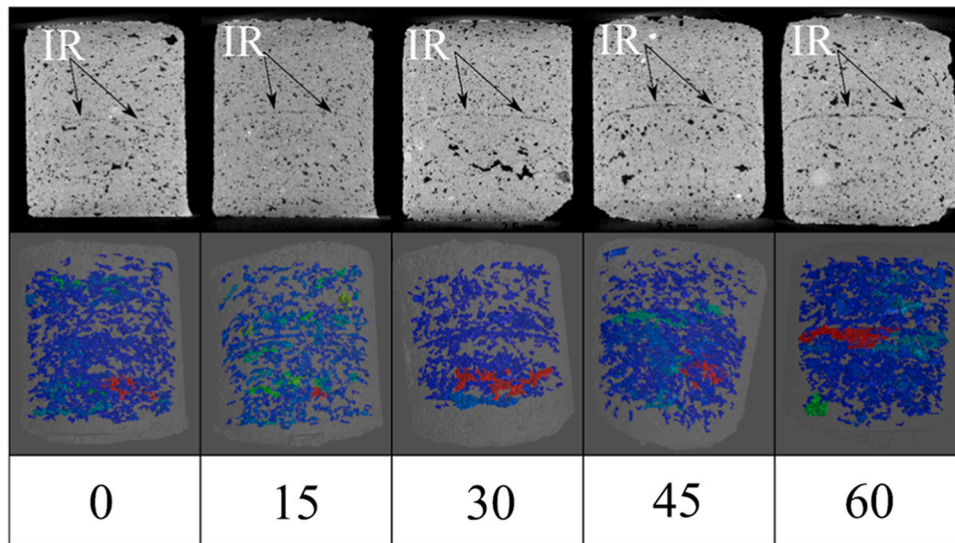


Fig. 10. CT images and 3D porosity renders of the 3D printed specimens, D20H20PH, for pass times ranging between 0 and 60 min.

pass times are significant such that they interconnect to form one large void. Air entrapment between filaments is not noted in this study, likely due to the overlay compaction realized with the correct print parameter combinations (deposition height/nozzle standoff distance, print speed, material extrusion rate, filament layer height) [28]. However, the severity of interlayer porosity presented here may not necessarily be extrapolated to and generalized for all printable mixtures, since various print parameters [6,28], material rheology characteristics (yield stress, viscosity and thixotropy) [35,36] and environmental or climatic conditions influencing evaporation and surface roughness of exposed filaments [37,38] collectively contribute toward interlayer porosity.

3.3. Vertical interlayer porosity

The porosity between laterally deposited filament layers is investigated via specimen D20H10PV, with the interlayer region oriented vertically. The CT results are depicted in Fig. 12. No clear vertical IR is observed in the CT images for this specimen; however, this result is not surprising since a 0 min pass time was employed. A similar result as for D20H20PH0 was thus expected. In the 3D porosity render, a large void indicated in red is observed close to the expected IR position. It is postulated that this resulted from air entrapment during the printing process since the void is seemingly located in the interlayer and not intralayer. Rhombus-shaped cavities may originate at the intersection of vertical and horizontal IRs due to the circular nozzle employed in this study [39], consequently being smearing into the form indicated in Fig. 12. The porosity across the specimen width is depicted in Fig. 13. A peak porosity of 8% is observed less than 2 mm to the right of the expected IR position, acting as further evidence to the postulation that this may be an entrapped void. However, due to rounding of the filament lateral edges when using a circular nozzle, investigating the vertical IR's porosity may prove to be a complicated task, as other factors such as the extent of lateral compaction may significantly influence not only the position and verticality of the expected IR, but also the degree of air entrapment.

3.4. Multiple interlayers porosity

The porosity over multiple IRs were investigated to determine if any notable water migration occurred. The CT results of the D20H40PH, with a 0-minute pass time, are depicted in Fig. 14. In this instance the IRs are slightly visible in the CT image, however, are not entirely clear. No significant voids are visible in the IRs from the 3D porosity render, but

rather a collection of smaller irregular voids. The bottom half of the specimen contains more voids than the top half, for which the authors currently have no explanation. One larger intralayer void is observed in the third filament layer and another, larger, flat void at the top of the specimen. This is evident in Fig. 14B where a pronounced spike in porosity is observed close to the specimen top. No clear trend is visible in the rest of the data.

The CT results of the VEL specimen are depicted in Fig. 15C. Although a 0-minute pass time was employed, the IRs are clearly visible between all filament layers, irrespective of the print speed utilized (80, 100 or 120 mm/s). The exact reason therefore remains unknown to the authors; however, it is postulated that the increased print speed reduces the overlay compaction effect and hence increasing porosity is evident at the IRs. These IRs are confirmed by the 3D porosity render, where it can be seen that the IRs consist of many small voids together with larger voids in the intralayers. An interesting observation is the visibly reduced number of voids located just below the bottom IR in the 3D render, likely due to water migration from new-to-old concrete [40,41]. This is also somewhat evident in the 3D render in Fig. 14A, however, complementary research is required to confirm this postulation. A further observation is noted in Fig. 15A, where an enormous intralayer void is seen just below the IR. Such void may drastically influence the hardened state mechanical properties of 3D printed concrete, not just due to its size, but also its proximity to the already-impaired IR. A last important observation made from this research, is that 3D printed concrete typically seems homogenous after being saw-cut, as is evident in Fig. 15B. No clear IR is present between filament layers on the specimen cross-section. However, evidence from the CT images in Fig. 15C indicate otherwise. It is thus incorrect to conclude that 3D printed concrete is homogenous if the premise is solely based on superficial photographic evidence.

Supplementary material related to this article can be found online at [doi:10.1016/j.addma.2020.101740](https://doi.org/10.1016/j.addma.2020.101740).

4. Conclusions

A comprehensive investigation of the microstructure – porosity in particular – of additive manufactured concrete elements by extrusion-based 3D printing is reported in this contribution. X-ray CT is used to explore the microscopic pore structure in the intra and interlayers, in comparison with reference specimens cast from the same concrete mix. Thereby, the influence of pumping and extrusion, as well as the additive, layered 3D printing process is quantified. Both horizontal and vertical

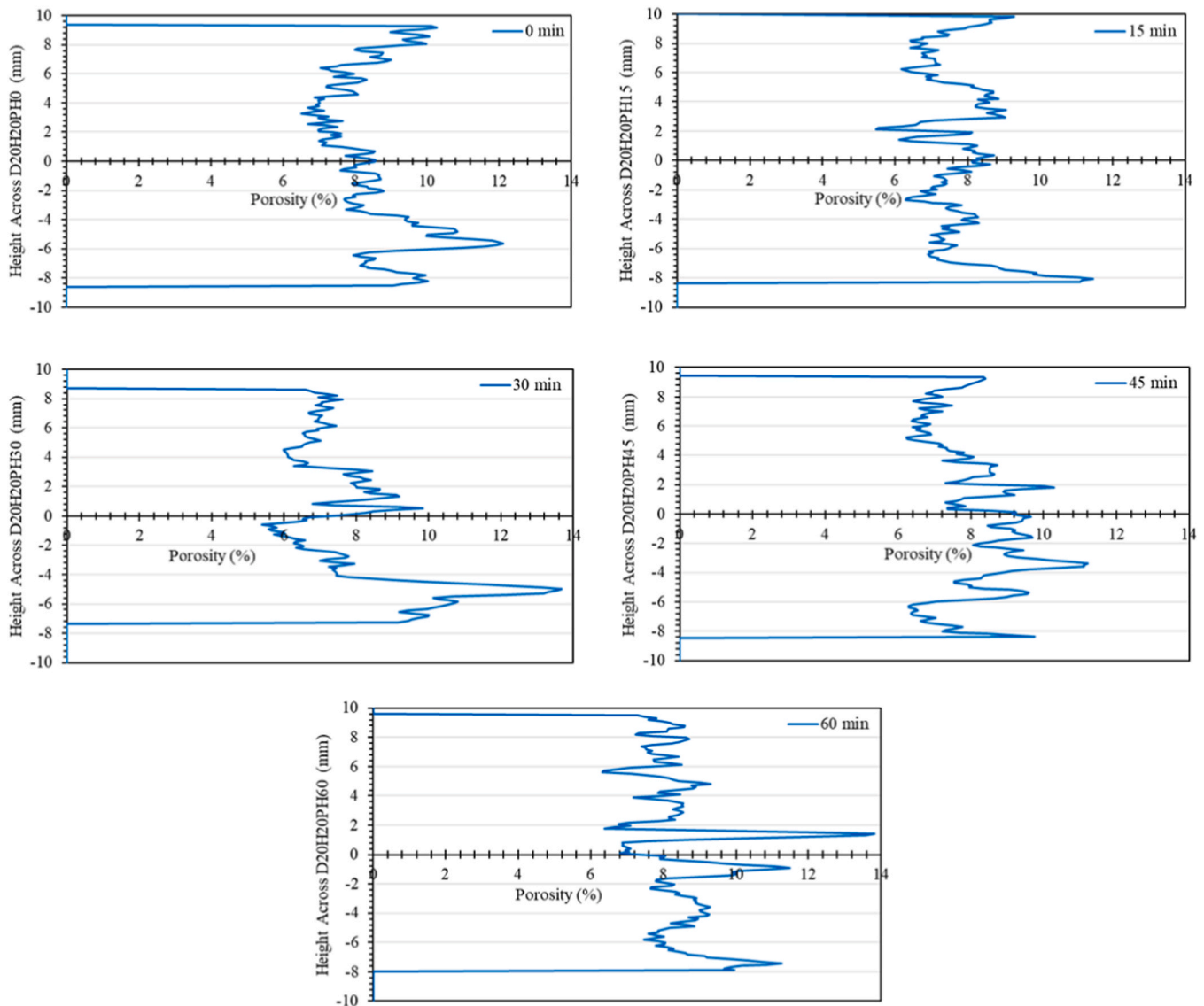


Fig. 11. Porosity percentage over the D20H20PH specimen height for printing pass times ranging between 0 and 60 min. The specimen interlayer positions are located approximately at the 0 mm mark.

interfaces are analyzed, as present in the additive manufactured height and width of 3D printed concrete elements. Whilst a single cement-based mix composition, deposition height, pump frequency and vertically oriented circular nozzle is maintained, the print parameters of nozzle speed and pass time are varied. Novel 3D printed plastic cylindrical molds are used for sampling specimens from single, double and four filament layers, to investigate the pore structure in a single layer, a single interlayer and multiple (three) interlayers.

From the presented results, the following main conclusions are drawn:

- Compared with dominantly spherical shaped voids in cast specimens, intralayer voids in 3D printed specimens are elongated, with largest dimension in the printed (x) direction, followed by the transverse (y) direction and the smallest in the vertical (z) direction. The elongation is most dominant for larger voids in the mm range, exhibited by high void compactness (void volume / encapsulating sphere volume) of micro-voids, but low compactness of larger pores > 1 mm in diameter.
- 3D printed specimens have an increased porosity (7.9%) at the largely entrained air void scale observed here, compared with

reference cast specimens (6.8%), at a CT scanning resolution of 15 μm .

- Elements containing vertical joints can be produced by 3D printing to similar porosity as horizontal joints, here 8.0% and 7.7% respectively.
- For the materials used here, the interfacial region does not significantly influence total intralayer porosity, i.e. intralayer and interlayer regions have similar porosities of an average 8% at smaller pass times. Porosity distribution over the height of two layered specimens with a single interface, as well as four layered specimens including three interfaces confirm this finding, albeit with irregular, spurious peak porosities of roughly $8 \pm 2\%$ but with local minima less than 5% and maxima approaching 14% at IRs.
- For pass times below 45 min, pore shape and size in the interlayer regions do not significantly differ from those in the intralayer. The region towards the undulating 3D printed edge (Fig. 1), excluded in the specimen sampling here, showed more elongated and interconnected pores in the intralayer in a previous investigation. For long pass times of 45 and 60 min, significantly elongated pores are observed in Fig. 10. It is acknowledged that the increasingly visible,

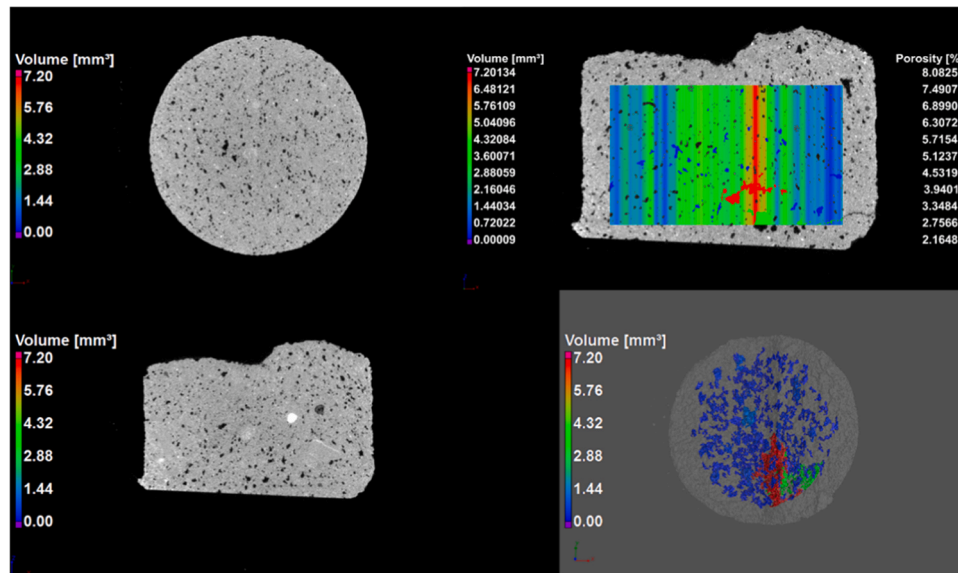


Fig. 12. The top and side CT images of the 3D printed specimen, D20H10PV, as well as a 3D render indicating void positions, shapes, distributions, and volumes. An overlay porosity map indicates the porosity across the specimen width, with the interlayer orientated vertically.

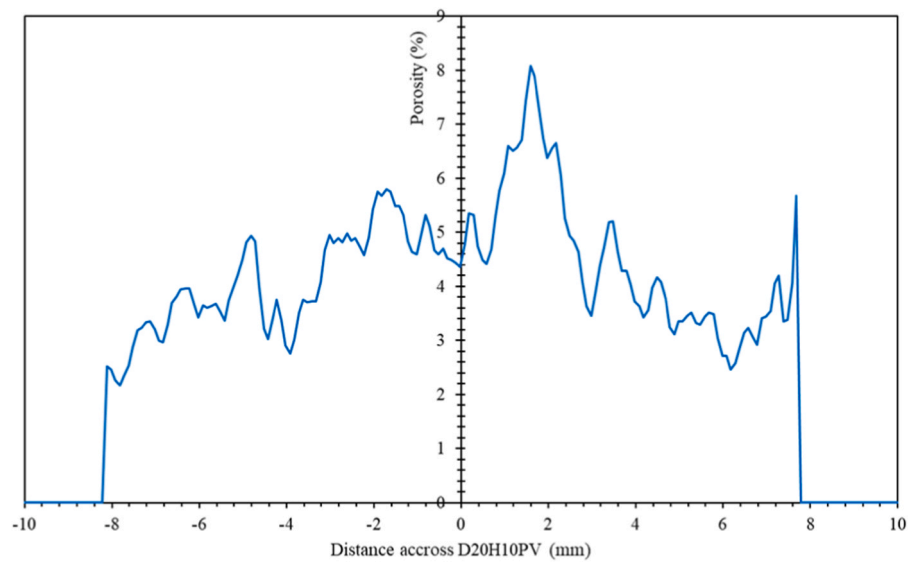


Fig. 13. Porosity percentage across the D20H10PV specimen width. The specimen's vertical interlayer position is located approximately at the 0 mm mark.

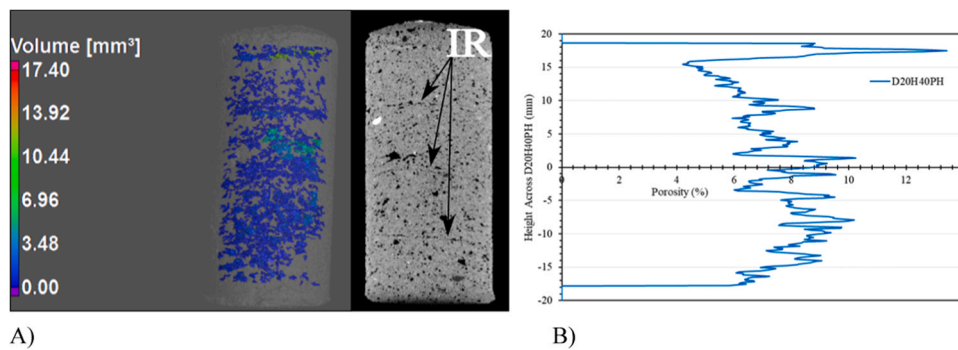


Fig. 14. A) 3D porosity render and CT image of the D20H40PH specimen and B) the porosity percentage over the height of the D20H40PH specimen.

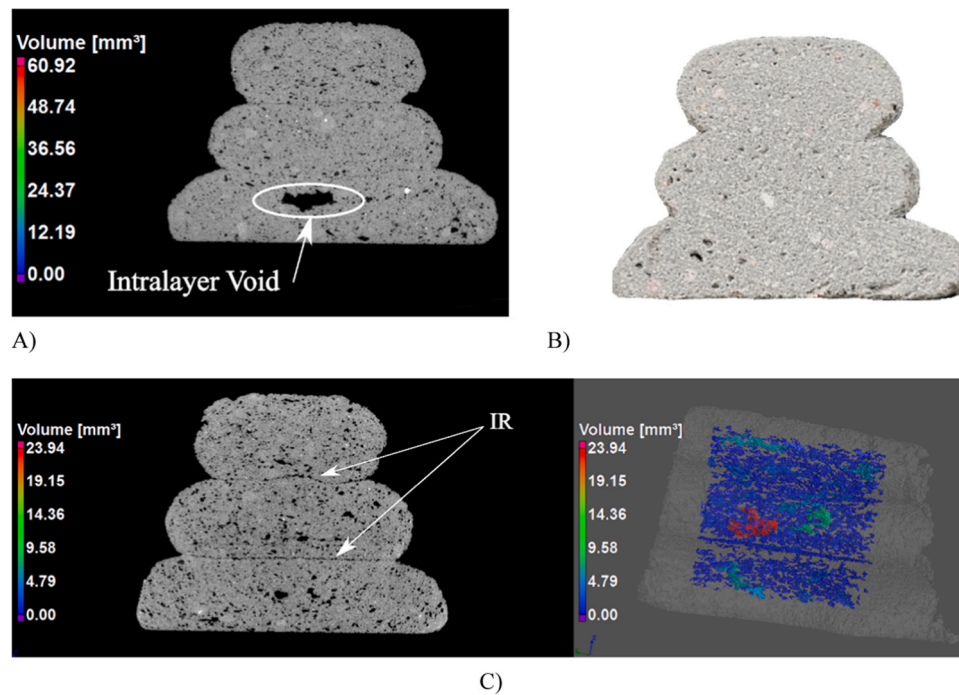


Fig. 15. A) CT image of the VEL specimen indicating a large intralayer void located just below the interlayer, B) a cross-sectional photo of a VEL specimen that was saw-cut and C) a cross-sectional CT image and 3D porosity render of the VEL specimen. A supplementary Video 2 is provided for visualization of (A).

hence discontinuous interface with longer pass times is here represented by elongated voids.

- In the print speed range of 80–120 mm/s used here, filament porosity is mostly unaffected. However, striking interfacial disconnection is caused by the increased nozzle speed, despite the zero-minute pass time in this case. This demands further investigation, postulated to be improved by appropriately higher, matching material extrusion rate.
- It is inaccurate to qualify the homogeneity of 3D printed concrete elements based solely on superficial cross-sectional photographic evidence from saw-cut samples. It is shown in this research (Fig. 15), that although a 3D printed concrete element may seem homogenous, it may not always be the case as visible IRs are present on the CT images.

For future research, it is recommended that capillary porosity properties of 3D printed concrete are determined, both intra- and interlayer, and compared to that of cast concrete, since these small pores may significantly contribute toward the overall mechanical and durability performance of concrete.

CRediT authorship contribution statement

Jacques Kruger: Conceptualization, Methodology, Validation, Investigation, Resources, Data curation, Writing - original draft, Writing - review & editing, Visualization, Project administration. **Anton du Plessis:** Conceptualization, Methodology, Software, Validation, Formal analysis, Investigation, Resources, Data curation, Writing - original draft, Writing - review & editing, Visualization, Funding acquisition. **Gideon van Zijl:** Formal analysis, Resources, Data curation, Writing - original draft, Writing - review & editing, Visualization, Supervision, Funding acquisition.

Declaration of Competing Interest

The authors declare the following financial interests/personal relationships which may be considered as potential competing interests:

One of the authors of this article is part of the editorial board of the journal. To avoid potential conflicts of interest, the responsibility for the editorial and peer-review process of this article lies with the other editors of the journal. Furthermore, the authors of this article were removed from the peer review process and have no access to confidential information related to the editorial process of this article.

Acknowledgements

The support by The Concrete Society in South Africa is gratefully acknowledged. Funding of Anton du Plessis through the South African Collaborative Program in Additive Manufacturing (CPAM) is thankfully acknowledged.

References

- [1] C. Menna, J. Mata-Falcón, F.P. Bos, G. Vantghem, L. Ferrara, D. Asprone, T. Salet, W. Kaufmann, Opportunities and challenges for structural engineering of digitally fabricated concrete, *Cem. Concr. Res.* 133 (2020), 106079, <https://doi.org/10.1016/j.cemconres.2020.106079>.
- [2] V. Mechtcherine, F.P. Bos, A. Perrot, W.R.L. da Silva, V.N. Nerella, S. Fataei, R.J. M. Wolfs, M. Sonebi, N. Roussel, Extrusion-based additive manufacturing with cement-based materials – production steps, processes, and their underlying physics: a review, *Cem. Concr. Res.* 132 (2020), 106037, <https://doi.org/10.1016/j.cemconres.2020.106037>.
- [3] J. Kruger, S. Cho, S. Zeranka, C. Viljoen, G. van Zijl, 3D concrete printer parameter optimisation for high rate digital construction avoiding plastic collapse, *Compos. Part B Eng.* 183 (2020), 107660, <https://doi.org/10.1016/j.compositesb.2019.107660>.
- [4] J.H. Jo, B.W. Jo, W. Cho, J.H. Kim, Development of a 3D printer for concrete structures: laboratory testing of cementitious materials, *Int. J. Concr. Struct. Mater.* 14 (2020) 13, <https://doi.org/10.1186/s40069-019-0388-2>.
- [5] T.T. Le, S.A. Austin, S. Lim, R.A. Buswell, R. Law, A.G.F. Gibb, T. Thorpe, Hardened properties of high-performance printing concrete, *Cem. Concr. Res.* 42 (2012) 558–566, <https://doi.org/10.1016/j.cemconres.2011.12.003>.
- [6] V.N. Nerella, S. Hempel, V. Mechtcherine, Effects of layer-interface properties on mechanical performance of concrete elements produced by extrusion-based 3D-printing, *Constr. Build. Mater.* 205 (2019) 586–601, <https://doi.org/10.1016/j.conbuildmat.2019.01.235>.
- [7] J. Van Der Putten, M. Azima, P. Van den Heede, T. Van Mullem, D. Snoeck, C. Carminati, J. Hovind, P. Trtik, G. De Schutter, K. Van, Neutron radiography to study the water ingress via the interlayer of 3D printed cementitious materials for continuous layering, *Constr. Build. Mater.* 258 (2020), 119587, <https://doi.org/10.1016/j.conbuildmat.2020.119587>.

- [8] J.G. Sanjayan, B. Nematollahi, M. Xia, T. Marchment, Effect of surface moisture on inter-layer strength of 3D printed concrete, *Constr. Build. Mater.* 172 (2018) 468–475, <https://doi.org/10.1016/j.conbuildmat.2018.03.232>.
- [9] J. Van Der Putten, M. Deprez, V. Cnudde, G. De Schutter, K. Van Tittelboom, Microstructural characterization of 3D printed cementitious materials, *Materials* 12 (2019) 2993, <https://doi.org/10.3390/ma12182993>.
- [10] J. Kruger, G. van Zijl, A compendious review on lack-of-fusion in digital concrete fabrication, *Addit. Manuf.* (2020), 101654, <https://doi.org/10.1016/j.addma.2020.101654>.
- [11] R.J.M. Wolfs, F.P. Bos, T.A.M. Salet, Hardened properties of 3D printed concrete: the influence of process parameters on interlayer adhesion, *Cem. Concr. Res.* 119 (2019) 132–140, <https://doi.org/10.1016/j.cemconres.2019.02.017>.
- [12] B. Anleu, Quantitative micro XRF mapping of chlorides: possibilities, limitations, and applications, from cement to digital concrete, *ETH Zur.* (2018), <https://doi.org/10.3929/ethz-a-010782581>.
- [13] J. Van Der Putten, M. De Volder, P. Van den Heede, G. De Schutter, K. Van Tittelboom, 3D Printing of Concrete: The Influence on Chloride Penetration, in: 2nd RILEM Int. Conf. Concr. Digit. Fabr., 2020: pp. 500–507. https://doi.org/10.1007/978-3-030-49916-7_51.
- [14] F. Bester, M. van den Heever, J. Kruger, S. Cho, G. van Zijl, Steel Fiber Links in 3D Printed Concrete in: Second RILEM Int. Conf. Concr. Digit. Fabr. - Digit. Concr. 2020/2020 Springer Eindhoven, The Netherlands 398 406 doi: 10.1007/978-3-030-49916-7_41. in: Second RILEM Conference: 2nd RILEM International Conference on Concrete and Digital Fabrication 2020.
- [15] A. Perrot, Y. Jacquet, D. Rangeard, E. Courteille, M. Sonebi, Nailing of layers: a promising way to reinforce concrete 3D printing structures, *Materials* 13 (2020) 1518, <https://doi.org/10.3390/ma13071518>.
- [16] J. Kruger, A. Cicone, F. Bester, M. van den Heever, S. Cho, R. Walls, G. van Zijl, Facilitating Ductile Failure of 3D Printed Concrete Elements in Fire, in: 2nd RILEM Int. Conf. Concr. Digit. Fabr., 2020: pp. 449–458. https://doi.org/10.1007/978-3-030-49916-7_46.
- [17] A. Cicone, J. Kruger, R.S. Walls, G. Van Zijl, An experimental study of the behavior of 3D printed concrete at elevated temperatures, In press, *Fire Saf. J.* (2020), 103075, <https://doi.org/10.1016/j.firesaf.2020.103075>.
- [18] H. Lee, J.H.J. Kim, J.H. Moon, W.W. Kim, E.A. Seo, Correlation between pore characteristics and tensile bond strength of additive manufactured mortar using X-ray computed tomography, *Constr. Build. Mater.* (2019) 712–720, <https://doi.org/10.1016/j.conbuildmat.2019.07.161>.
- [19] D. Winslow, D. Liu, The pore structure of paste in concrete, *Cem. Concr. Res.* 20 (1990) 227–235, [https://doi.org/10.1016/0008-8846\(90\)90075-9](https://doi.org/10.1016/0008-8846(90)90075-9).
- [20] D. Liu, B. Šavija, G.E. Smith, P.E.J. Flewitt, T. Lowe, E. Schlangen, Towards understanding the influence of porosity on mechanical and fracture behaviour of quasi-brittle materials: experiments and modelling, *Int. J. Fract.* 205 (2017) 57–72, <https://doi.org/10.1007/s10704-017-0181-7>.
- [21] H.W. Chandler, L.J. Merchant, R.J. Henderson, D.E. Macphie, Enhanced crack-bridging by unbonded inclusions in a brittle matrix, *J. Eur. Ceram. Soc.* 22 (2002) 129–134, [https://doi.org/10.1016/S0955-2219\(01\)00242-4](https://doi.org/10.1016/S0955-2219(01)00242-4).
- [22] A. du Plessis, W.P. Boshoff, A review of X-ray computed tomography of concrete and asphalt construction materials, *Constr. Build. Mater.* 199 (2019) 637–651, <https://doi.org/10.1016/j.conbuildmat.2018.12.049>.
- [23] A. Du Plessis, I. Yadroitsev, I. Yadroitsava, S.G. Le Roux, X-ray microcomputed tomography in additive manufacturing: a review of the current technology and applications, 3D print, *Addit. Manuf.* 5 (2018) 227–247, <https://doi.org/10.1089/3dp.2018.0060>.
- [24] J. Kruger, S. Zeranka, G.P.A.G. van Zijl, An ab initio approach for thixotropy characterisation of nanoparticle-infused 3D printable concrete, *Constr. Build. Mater.* 224 (2019) 372–386, <https://doi.org/10.1016/j.conbuildmat.2019.07.078>.
- [25] P.J. Kruger, M. van den Heever, S. Cho, S. Zeranka, G. van Zijl, High-Performance 3D Printable Concrete Enhanced With Nanomaterials (in: Proc. International Conference on Sustainable Materials, Systems and Structures 2019 RILEM Publications S.A.R.L. Rovinj, Croatia 533 540. (in: Proc. Int. Conf. Sustain. Mater. Syst. Struct. New Gener. Constr. Mater.).
- [26] J. Kruger, S. Zeranka, G. van Zijl, 3D concrete printing: a lower bound analytical model for buildability performance quantification, *Autom. Constr.* 106 (2019), 102904, <https://doi.org/10.1016/j.autcon.2019.102904>.
- [27] A. du Plessis, B.J. Olawuyi, W.P. Boshoff, S.G. le Roux, Simple and fast porosity analysis of concrete using X-ray computed tomography, *Mater. Struct. Constr.* 49 (2016) 553–562, <https://doi.org/10.1617/s11527-014-0519-9>.
- [28] B. Panda, N.A.N. Mohamed, S.C. Paul, G.V.P.B. Singh, M.J. Tan, B. Šavija, The effect of material fresh properties and process parameters on buildability and interlayer adhesion of 3D printed concrete, *Materials* 12 (2019) 2149, <https://doi.org/10.3390/ma12132149>.
- [29] G.M. Moelich, J. Kruger, R. Combrinck, Plastic shrinkage cracking in 3D printed concrete, *Compos. Part B Eng.* 200 (2020), 108313, <https://doi.org/10.1016/j.compositesb.2020.108313>.
- [30] A. du Plessis, P. Sperling, A. Beerlink, L. Tshabalala, S. Hoosain, N. Mathe, S.G. le Roux, Standard method for microCT-based additive manufacturing quality control 1: porosity analysis, *MethodsX* 5 (2018) 1102–1110, <https://doi.org/10.1016/j.mex.2018.09.005>.
- [31] S. Talukdar, R. Heere, The effects of pumping on the air content and void structure of air-entrained, wet mix fibre reinforced shotcrete, *Case Stud. Constr. Mater.* 11 (2019), e00288, <https://doi.org/10.1016/j.cscm.2019.e00288>.
- [32] H. Kloft, H.W. Krauss, N. Hack, E. Herrmann, S. Neudecker, P.A. Varady, D. Lowke, Influence of process parameters on the interlayer bond strength of concrete elements additive manufactured by Shotcrete 3D Printing (SC3DP), *Cem. Concr. Res.* 134 (2020), 106078, <https://doi.org/10.1016/j.cemconres.2020.106078>.
- [33] A.A. Griffith, The Phenomena of Rupture and Flow in Solids, *Philos. Trans. R. Soc. Lond. Ser. A Contain. Pap. A Math. Or. Phys. Character* 221 (1920) 163–198. https://www.jstor.org/stable/91192?seq=1#metadata.info_tab_contents.
- [34] A. Roberts, Geotechnology: Chapter 4 - Failure Criteria for Soils and Rocks, Elsevier, 1977, pp. 51–53, <https://doi.org/10.1016/C2013-0-05711-8> (in:).
- [35] K. Kim, S. Park, W.S. Kim, Y. Jeong, J. Lee, Evaluation of shear strength of RC beams with multiple interfaces formed before initial setting using 3D printing technology, *Materials* 10 (2017) 1349, <https://doi.org/10.3390/ma10121349>.
- [36] Y.W.D. Tay, G.H.A. Ting, Y. Qian, B. Panda, L. He, M.J. Tan, Time gap effect on bond strength of 3D-printed concrete, *Virtual Phys. Prototyp.* 14 (2019) 104–113, <https://doi.org/10.1080/17452759.2018.1500420>.
- [37] E. Keita, H. Bessaies-Bey, W. Zuo, P. Belin, N. Roussel, Weak bond strength between successive layers in extrusion-based additive manufacturing: measurement and physical origin, *Cem. Concr. Res.* 123 (2019), 105787, <https://doi.org/10.1016/j.cemconres.2019.105787>.
- [38] Y. He, X. Zhang, R.D. Hooton, X. Zhang, Effects of interface roughness and interface adhesion on new-to-old concrete bonding, *Constr. Build. Mater.* 151 (2017) 582–590, <https://doi.org/10.1016/j.conbuildmat.2017.05.049>.
- [39] M. Moini, J. Olek, B. Magee, P. Zavattieri, J. Youngblood, Additive Manufacturing and Characterization of Architected Cement-Based Materials via X-ray Micro-computed Tomography BT - First RILEM International Conference on Concrete and Digital Fabrication - Digital Concrete 2018, 2019 176–189.
- [40] M. Lukovic, G. Ye, Effect of moisture exchange on interface formation in the repair system studied by X-ray absorption, *Mater. Basel* 9 (2016), <https://doi.org/10.3390/ma9010002>.
- [41] M. Lukovic, G. Ye, E. Schlangen, K. Van, Breugel, Moisture movement in cement-based repair systems monitored by X-ray absorption, *Heron* 62 (2017) 21–46.